scientific reports

Check for updates

OPEN

MIL-53(Al)-derived bimetallic Pd–Co catalysts for the selective hydrogenation of 1,3-butadiene at low temperature

Lili Liu✉, Miaoliang Zang, Lei Li, Yunkai Zhang, Leyuan Wang, Xiaojing Zhou, Chunling Xin✉ & Xishi Tai✉

Selective hydrogenation of 1,3-butadiene is a crucial industrial process for the removing of 1,3-butadiene, a byproduct of butene production. Developing catalysts with high catalytic performance for the hydrogenation of 1,3-butadiene at low temperatures has become a research hotspot. In this study, bimetallic Pd–Co catalysts supported on Al_2O_3 derived from MIL-53(Al) at various calcination temperatures were synthesised via the co-impregnation method. These catalysts were structurally characterised using powder X-ray diffraction, thermogravimetric analysis, N_2 adsorption–desorption, X-ray photoelectron spectroscopy, transmission electron microscopy, energy-dispersive X-ray spectroscopy, and inductively coupled plasma optical emission spectroscopy techniques. The characterisations revealed that Pd–Co nanoparticles, averaging 8.5–12.4 nm, were highly dispersed on Al_2O_3 derived from MIL-53(Al). The effects of reaction temperature, Pd and Co contents, space velocity, and calcination temperature on the catalytic performance for the hydrogenation of 1,3-butadiene were thoroughly investigated. The PdCo/MIL-53(Al)-A700 catalyst exhibited the highest catalytic activity for the hydrogenation of 1,3-butadiene at 40 °C and a space velocity of 900 L/(h·g_{cat}). This catalyst demonstrated a strong synergistic interaction between Pd and Co nanoparticles, resulting in considerably better catalytic performance than the monometallic Pd catalyst under the same conditions. The PdCo/MIL-53(Al)-A700 catalyst achieved superior 1,3-butadiene conversion and total butene selectivity compared to the Pd/MIL-53(Al)-A700 catalyst. In addition, the PdCo/MIL-53(Al)-A700 catalyst maintained its catalytic activity and total butene selectivity after three regenerations in a flow of N_2 at 200 °C. This work proposed a new pathway to design efficient and sustainable catalysts for 1,3-butadiene hydrogenation.

Keywords MIL-53(Al), Derived, Pd–Co, Bimetallic catalysts, 1,3-Butadiene

Butenes are a valuable component in the chemical industry used in coatings, rubber, plastics, and other high-value chemicals[1]. The primary method for producing butenes is the catalytic cracking of crude oil[2,3]. However, this process generates 1,3-butadiene as a byproduct, which must be reduced to below 10 ppm before downstream reaction processing[3–5]. Because 1,3-butadiene not only made subsequent product separation difficult, but also poisoned the catalysts[3–5]. Selective hydrogenation of 1,3-butadiene to produce butenes is a promising method for removing residual 1,3-butadiene from butene-rich streams[6,7]. Transition metal palladium (Pd) exhibits high reactivity in the hydrogenation of 1,3-butadiene owing to the low barrier of H_2 dissociation energy (~0 eV), making it a widely used catalyst for this reaction[7–9]. However, monometallic Pd catalysts often have low selectivity for butenes (1-butene, *trans*-2-butene, and *cis*-2-butene) at high conversion of 1,3-butadiene, resulting in overhydrogenation and the formation of undesired byproducts such as butane[10–12]. Therefore, developing novel catalysts to enhance selectivity is essential for the hydrogenation of 1,3-butadiene. Strategies to improve the selectivity of the catalyst, include using tuned supports[13,14], constructing nanostructures[15,16], modifying with ionic liquid layers[17,18], second employing bimetallic[19–21] or single-atom catalsyts[22,23]. Bimetallic catalysts are widely recognised for their enhanced catalytic activity and selectivity. Various Pd-based bimetallic catalysts have been designed and used, including Pd–Ag[4,24], Pd–Au[21,25], Pd–Ni[26,27], Pd–Cu[28,29], Pd–Zn[14], and Pd–Sn[30] for the hydrogenation of 1,3-butadiene. These bimetallic catalysts demonstrate superior performance compared to

School of Chemistry & Chemical Engineering and Environmental Engineering, Weifang University, Weifang 261061, China. ✉email: liulili122@126.com; xinchunling0925@126.com; taixs@wfu.edu.cn

monometallic Pd catalysts[28–30]. For instance, Corestius et al.[28] reported that Pd–Cu bimetallic catalysts achieved high butene selectivities (over 75%) at a 1,3-butadiene conversion of 90%. Specifically, the $Pd_{13}Cu_{87}$/C catalyst with 0.5 wt% Pd loading exhibited a butene selectivity of 78%, outperforming the 62% selectivity of the 0.5 wt% monometallic Pd/C catalyst[28]. Ma et al.[24] discovered that adding Ag to Pd surfaces can weaken the adsorption of 1-butene and 1,3-butadiene, thereby enhancing the catalytic activity and selectivity for the hydrogenation of 1,3-butadiene to 1-butene. Additionally, Au(2)Pd(1)/MIL-101(Cr) bimetallic catalysts exhibited a considerably higher butene selectivity (95.7%) at nearly 100% conversion of 1,3-butadiene, compared to the monometallic Pd/MIL-101(Cr) catalysts, which achieved only 63.3% selectivity[31].

Cobalt is a good adatom candidate because it is low-cost and has a good effect on Pd metal[32]. In recent years, bimetallic Pd–Co catalysts have been widely studied and exhibited good performances in catalytic hydrogenation[33]. Li et al.[33] reported that PdCo/CNC-2.5 catalyst exhibited excellent catalytic activity with TOF value of 2570 h^{-1} and 94.1% selectivity of 3-ethylnitrobenzene in methanol under 3 bar H_2 at 50 °C for the selective hydrogenation of 3-nitrostyrene. The improved hydrogenation performance for PdCo/CNC-2.5 can be ascribed to the synergistic effect of PdCo[33]. Moreover, compared with Pd/CNC catalyst, PdCo/CNC-2.5 catalyst exhibited a relative low reaction barrier for selective hydrogenation of 3-nitrostyrene[33]. Luo et al.[34] demonstrated that Pd/Co catalyst exhibited excellent good catalytic performance for the hydrogenation of nitrobenzene. The yield of aniline was 99%, and the catalytic activity was 158 times than that of commercial Pd powder[34].

In practice, the metal nanoparticles are easily attracted each other and aggregate into larger naoparticles due to the magnetic force and van der Waals forces, which could greatly reduce the reactivity and affect the stability of metal nanoparticles[35]. Dispersing metal nanoparticles on the support can control the migration and aggregation of the metal nanoparticles, thereby further increase their catalytic activity and stability[36]. Several supporters have been used to stabilized metal nanoparticles, including metal–organic framework (MOF)[37], ploymer[38], metal oxide[39], carbon microsphere[40], carbon cloth[41], and graphene[42]. Among them, MOFs have attracted growing attention as heterogeneous catalysts owing to their unique structural characteristics including high porosity, large specific surface areas, well-defined metal nodes, tunable topologies and controlled pore sizes[43–50]. However, the poor stability of the MOFs has considerably limited their application in many catalytic processes. MOF-derived materials produced through simple pyrolysis method using MOFs as templates or precursors not only address the stability issues but also retain the structural advantages of MOFs, thereby greatly expanding their applications in catalytic reactions[51]. For instance, Li et al.[52] reported that Ni nanoparticles supported on MIL-125(Ti)-derived TiO_2 displayed excellent catalytic performance for CO_2 methanation, achieving a maximum CH_4 production rate of 463.9 mmol/(g_{Ni}·h) with nearly 100% selectivity under IR irradiation (1530 mW/cm^2) and maintaining durability for at least 48 h[52]. Additionally, Jia et al.[53] developed a hierarchically porous iridium catalyst supported by ZrO_2 derived from MOFs (Ir-N@HP-mesoZrO_2) and successfully applied it to the construction of julolidines via the reductive annulation of quinolines and conjugated enones[53]. The Ir-N@HP-mesoZrO_2-350 catalyst demonstrated reusability for at least six cycles at half conversion, with only a slight decrease in activity observed after the fifth cycle[53]. Mei et al.[54] also reported that the CeO_2–C catalyst, prepared by pyrolysing a Ce–MOF template with the assistance of cetyltrimethylammonium bromide, displayed excellent low-temperature catalytic activity for the oxidation of o-xylene. Additionally, the CeO_2–C catalyst demonstrated good thermal stability in long-term tests (30 h) and water resistance[54]. In this work, a series of bimetallic Pd–Co catalysts supported on MIL-53(Al)-derived Al_2O_3, synthesised via the co-impregnation method at different calcination temperatures, were investigated for the selective hydrogenation of 1,3-butadiene. The effects of reaction temperature, Pd and Co contents, space velocity and calcination temperature on the catalytic performance for 1,3-butadiene hydrogenation were systematically studied. In addition, the stability and regeneration capability of the catalyst were also studied in detail. Benefiting from bimetallic synergistic effects, bimetallic catalyst PdCo/MIL-53(Al)-A700 exhibited excellent 1,3-butadiene hydrogenation performance than monometallic catalyst Pd/MIL-53(Al)-A700. The degradation for PdCo/MIL-53(Al)-A700 was mainly ascribed to the carbon deposition on the catalyst. Moreover, the catalyst PdCo/MIL-53(Al)-A700 could be easily regenerated in a flow of N_2 at 200 °C.

Experimental section

Preparation of catalysts

Synthesis of Al_2O_3 derived from MIL-53(Al)

MIL-53(Al) was synthesised using a modified solvothermal methods[55]. $Al(NO_3)_3·9H_2O$ (21.00 mmol, 7.80 g) and terephthalic acid (H_2BDC, 7.00 mmol, 1.15 g) were dissolved in 10 mL of water under stirring at 500 rpm for 0.5 h. The resulting mixture transferred to a 100 mL Teflon-lined stainless steel autoclave and subjected to a solvothermal reaction at 493 K for 72 h. The resulting white powder of MIL-53(Al) was isolated by centrifugation (4000 rpm, 20 min) and washed three times with 15 mL of absolute ethanol. Additionally, the material was refluxed in ethanol (100 mL) at 100 °C for 24 h. The obtained products were dried in a vacuum oven at 150 °C for 12 h to yield the MIL-53(Al) precursors. The dried MIL-53(Al) was then calcined in air atmosphere at 500 °C–800 °C for 3 h, with a heating rate of 2 °C/min using a muffle furnace. The resulting solids were labelled as MIL-53(Al)-AT, where A is the calcination atmosphere (air) and T is the calcination temperature.

Synthesis of catalysts

The PdCo/MIL-53(Al)-AT catalysts were synthesised using the co-impregnation method. Palladium chloride ($PdCl_2$, 4.40 mg, 0.025 mmol) and cobalt nitrate hexahydrate ($Co(NO_3)_2·6H_2O$, 12.8 mg, 0.044 mmol) were dissolved in 1.5 mL of absolute ethanol and sonicated at room temperature for 30 min. This ethanol solution of $PdCl_2$ and $Co(NO_3)_2·6H_2O$ was then added dropwise to 50.00 mg of MIL-53(Al)-A700, and the mixture was continuously sonicated for an additional 30 min at room temperature. After ageing overnight, the resulting solids were dried at 100 °C for 1 h under vacuum (0.1 MPa). Finally, the dried product was reduced at 100 °C

for 2 h under a hydrogen flow (12.0 mL/min). The resulting solids were designated as PdCo/MIL-53(Al)-A700. The other catalysts, PdCo/MIL-53(Al)-A500, PdCo/MIL-53(Al)-A600, PdCo/MIL-53(Al)-A800-1, PdCo/MIL-53(Al)-A800-2, and PdCo/MIL-53(Al)-A800-3 were prepared using the same method. For comparison, the Pd/MIL-53(Al)-A700 catalyst was synthesised using $PdCl_2$ as the precursor, without $Co(NO_3)_2{\cdot}6H_2O$. The catalysts were stored at 4℃ under atmospheric environment without any passivation treatment after the reduction in the final stage of catalyst preparation. The metal weight percentages (Pd and Co) were determined using inductively coupled plasma optical emission spectroscopy (ICP–OES) (Table S1).

Catalytic activity evaluation

The catalytic performance of the prepared catalysts for the selective hydrogenation of 1,3-butadiene was evaluated. The hydrogenation reactions were performed in a fixed-bed flow reactor under atmospheric pressure. The temperature of the selective hydrogenation reaction was measured with a Cr-Al thermocouple located in the center of the catalyst bed. The reaction temperatures ranged from 20 °C to 40 °C with a fluctuation of 1 °C. For each test, 0.005 g of catalyst in a powder form was well mixed with 0.5 g of quartz sand (40–80 mesh) as a diluent, and then the mixture was loaded into the central section of the fixed-bed reactor. The temperature of the catalyst was increased at a rate of 2 °C/min using N_2 (99.99%, 12 mL/min) until the desired reaction temperature was achieved. Once the target temperature was reached, 1.0 vol% 1,3-butadiene in N_2 (20 mL/min) was premixed with H_2 (99.99%, 10 mL/min) in a buffer tank and then passed through the catalyst bed. N_2 was used as balance gas because it can greatly increase the space velocity of the catalytic reaction. The considerable mass transfer limitation of hydrogenation reaction was excluded by using high space velocity[56]. The reactor effluent was analysed using an online SP-6890 gas chromatograph (GC, Shandong Lunan Ruihong Chemical Engineering Instrument Co. Ltd., Shandong, China) equipped with an Al_2O_3 capillary column (30 m × 0.53 mm × 10 mm) and a flame ionisation detector. Samples of the reactor effluent were taken every 15 min and analysed with the GC. The conversions of 1,3-butadiene and the selectivities for butane, 1-butene, *trans*-2-butene, and *cis*-2-butene were determined based on the GC peak areas corresponding to the reactants and products. Stability experiments for PdCo/MIL-53(Al)-A700 were performed at 40 °C for 120 h to assess catalyst durability under reaction conditions. The stability tests were performed under the same experimental conditions as described above.

Results and discussion

Structural and morphological characterizations

The PXRD patterns of the samples were analysed and are shown in Fig. 1, which includes MIL-53(Al), MIL-53(Al)-AT, PdCo/MIL-53(Al)-AT, and Pd/MIL-53(Al)-A700 (T = 500 °C–800 °C). The PXRD pattern of MIL-53(Al) closely matches those reported in previous studies, confirming that the as-synthesised sample retains the MIL-53(Al) structure (Fig. 1a)[55,57]. The pattern features sharp and well-defind diffraction peaks, indicating high crystallinity of MIL-53(Al). The diffraction peaks at 2θ = 8.48°, 9.23°, 12.21° and 24.74° for MIL-53(Al)-A500 are similar to those observed for MIL-53(Al) (Fig. 1b). The intensity of the typical peaks at 9.38° and 12.21° for MIL-53(Al)-A500 considerably increased after thermal pyrolysis at 500 °C for 3 h in an air atmosphere (Fig. 1b). However, the diffraction peaks of MIL-53(Al) at 2θ = 9.98°, 14.15°, 14.89°, 16.83°, 18.19°, 20.27°, 21.77° and 23.99° disappeared after pyrolysis at 500 °C, indicating a decrease in the crystallinity of MIL-53(Al)-A500. The PXRD patterns of MIL-53(Al)-A600, MIL-53(Al)-A700 and MIL-53(Al)-A800 show substantial differences compared to that of MIL-53(Al) (Fig. 1c–e). New diffraction peaks at 2θ = 26.8°, 40.1°, 45.7° and 67.20° appear in these samples. The peak at 2θ = 26.8° corresponds to θ-Al_2O_3, while the peaks at 2θ = 40.1°, 45.7° and 67.20°

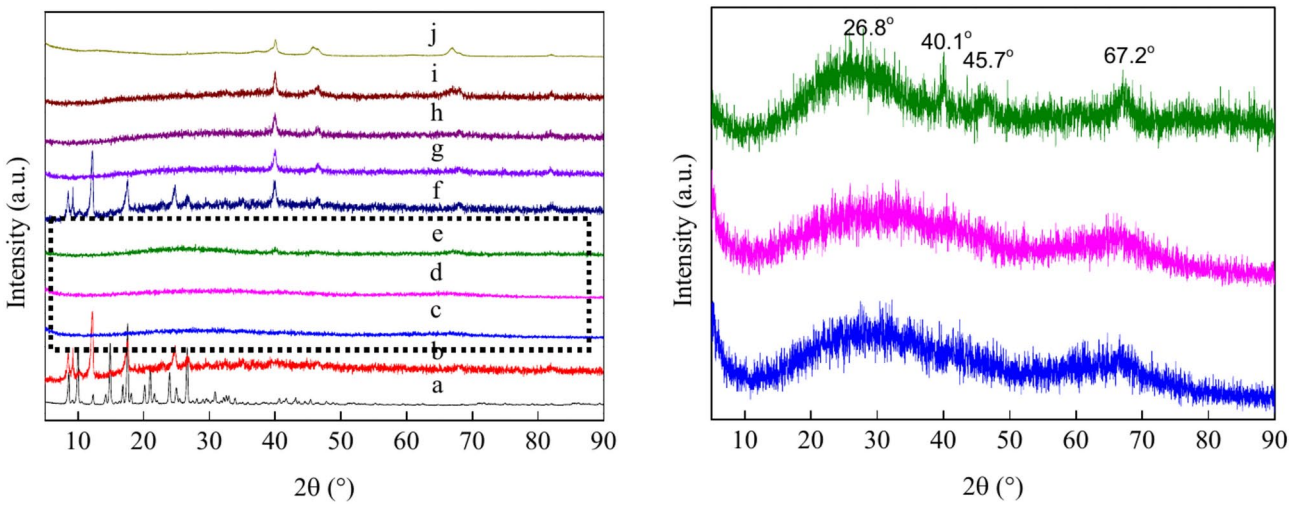

Fig. 1. The PXRD patterns of the samples: (**a**) MIL-53(Al); (**b**) MIL-53(Al)-A500; (**c**) MIL-53(Al)-A600; (**d**) MIL-53(Al)-A700; (**e**) MIL-53(Al)-A800; (**f**) PdCo/MIL-53(Al)-A500; (**g**) PdCo/MIL-53(Al)-A600; (**h**) PdCo/MIL-53(Al)-A700; (**i**) PdCo/MIL-53(Al)-A800-3; (**j**) Pd/MIL-53(Al)-A700.

are characteristic of γ-Al_2O_3[58–61]. Based on the PXRD diffraction patterns, a mixture of θ-Al_2O_3 and γ-Al_2O_3 was obtained by thermally pyrolysing MIL-53(Al) at 600 °C–800 °C for 3 h in an air atmosphere. The results indicated that MIL-53(Al) retained its original structure after pyrolysis at 500℃ for 3 h but fully decomposed into Al_2O_3 after pyrolysis at 600 °C–800℃ for 3 h. TGA of MIL-53(Al) showed that the material remained stable up to 550 °C (Fig. S1). This result is consistent with the PXRD data. After loading the bimetallic Pd–Co nanoparticles, the PdCo/MIL-53(Al)-AT catalysts (T = 500 °C–800 °C) exhibited four additional peaks at 2θ = 39.88°, 46.51°, 68.12° and 82.07°, which correspond to the (111), (200), (220) and (311) planes of the face-centred cubic (fcc) structure of PdCo alloy, respectively (Fig. 1f–i)[62–64]. In contrast, the PXRD diffraction peaks for Pd/MIL-53(Al)-A700 at 2θ = 39.99°, 45.89°, 66.93° and 82.02° (JCPDS 00–005-0681) were attributed to the (111), (200), (220) and (311) planes of metallic Pd (Pd^0), respectively[65,66].

The N_2 adsorption–desorption isotherms for MIL-53(Al), MIL-53(Al)-AT and PdCo/MIL-53(Al)-AT (T = 500 °C, 600 °C, 700 °C, and 800 °C) are shown in Figs. S2 and 2. The isotherms of MIL-53(Al) showed a typical IV isotherm, revealing that MIL-53(Al) possessed mesoporosity (Fig. S2)[67]. The BET surface area of MIL-53(Al) was 902 m^2/g. Huang et al.[67] reported that the BET surface area of MIL-53(Al) synthesised by hydrothermal method at 220 °C for 3d using H_2O as solvent was 915 m^2/g. The BET surface area of MIL-53(Al) synthesised by solvothermal method at 150 °C for 3d in DMF was 564 m^2/g[68]. The BET value of this work was consistent with that synthesised by hydrothermal method in H_2O, but it was higher than that synthesised by solvothermal method in DMF[67,68]. MIL-53(Al)-AT and PdCo/MIL-53(Al)-AT (T = 500 °C, 600 °C, 700 °C, and 800 °C) samples exhibited a typical type IV isotherm with an H4-shaped hysteresis loop at a relative pressure between 0.45 and 1.0, indicating the presence of uniform slit-shaped pores (Fig. 2)[69,70]. The substantial decrease in N_2 adsorption for PdCo/MIL-53(Al)-A500, PdCo/MIL-53(Al)-A600, PdCo/MIL-53(Al)-A700, and PdCo/MIL-53(Al)-A800-3 after the addition of Pd–Co alloy nanoparticles suggests that the pores of MIL-53(Al)-A500, MIL-53(Al)-A600, MIL-53(Al)-A700, and MIL-53(Al)-A800 were occupied or blocked by these nanoparticles (Fig. 2)[26,71]. The specific surface area was assessed using the BET method, while the total pore volume and average pore size were determined from the adsorption branch using the BJH method. Table S2 summaries the BET surface area, total pore volume, and the average pore diameter for all samples. The BET surface areas were measured as 438.6 m^2/g for MIL-53-A500, 133.0 m^2/g for MIL-53-A600, 121.6 m^2/g for MIL-53-A700 and 93.7 m^2/g for MIL-53(Al)-A800. The total pore volumes were 0.19 cm^3/g for MIL-53-A500, 0.47 cm^3/g for MIL-53-A600, 0.42 cm^3/g for MIL-53-A700 and 0.42 cm^3/g for MIL-53(Al)-A800. The average pore diameters were 8.5 nm for MIL-53-A500, 16.0 nm for MIL-53-A600, 15.0 nm for MIL-53-A700 and 17.5 nm for MIL-53(Al)-A800. These results indicate that the calcination temperature considerably affects the BET surface area, total pore volume and average pore diameter. MIL-53(Al)-A800 exhibited the smallest BET surface area at 93.7 m^2/g. The BET surface areas were 79.0 m^2/g for PdCo/MIL-53(Al)-A500, 123.0 m^2/g for PdCo/MIL-53(Al)-A600, 103.1 m^2/g for PdCo/MIL-53(Al)-A700 and 82.8 m^2/g for PdCo/MIL-53(Al)-A800-3. The BET surface area decreased upon loading Pd–Co alloy nanoparticles. The total pore volumes were 0.12 m^2/g for PdCo/MIL-53(Al)-A500, 0.49 m^2/g for PdCo/MIL-53(Al)-A600, 0.37 m^2/g for PdCo/MIL-53(Al)-A700 and 0.42 m^2/g for PdCo/MIL-53(Al)-A800-3. The average pore diameters were 17.0 nm for PdCo/MIL-53(Al)-A500, 15.0 nm for PdCo/MIL-53(Al)-A600, 15.1 nm for PdCo/MIL-53(Al)-A700 and 21.1 nm for PdCo/MIL-53(Al)-A800-3.

XPS was used to analyse the chemical states of Pd and Co species. Figure 3 and Fig. S3 show the XPS spectra for PdCo/MIL-53(Al)-A700 and Pd/MIL-53(Al)-A700. In the Pd 3d XPS spectra for PdCo/MIL-53(Al)-A700, peaks appeared at 340.7 and 335.3 eV, corresponding to the Pd^0 $3d_{3/2}$ and Pd^0 $3d_{5/2}$, respectively (Fig. 3a)[26,31,72]. The binding energy peaks at 346.3 eV and 337.1 eV were attributed to Pd^{2+} $3d_{3/2}$ and Pd^{2+} $3d_{5/2}$, respectively (Fig. 3a)[73,74]. The XPS spectra for Pd 3d indicated that Pd species in the PdCo/MIL-53(Al)-A700 catalyst were present as both Pd^0 and Pd^{2+}. The molar ratio of Pd^0:Pd^{2+} was estimated to be 2.7:1 based on the peak area. Pd/MIL-53(Al)-A700 exhibited only two peaks at 340.4 and 335.0 eV corresponding to Pd^0 $3d_{3/2}$ and Pd^0 $3d_{5/2}$, respectively (Fig. S3)[26,31,72]. The Pd species in the Pd/MIL-53(Al)-A700 catalyst were primarily in form of Pd^0. PdCo/MIL-53(Al)-A700 showed a 0.3 eV positive shift for the Pd^0 species compared to Pd/MIL-53(Al)-A700.

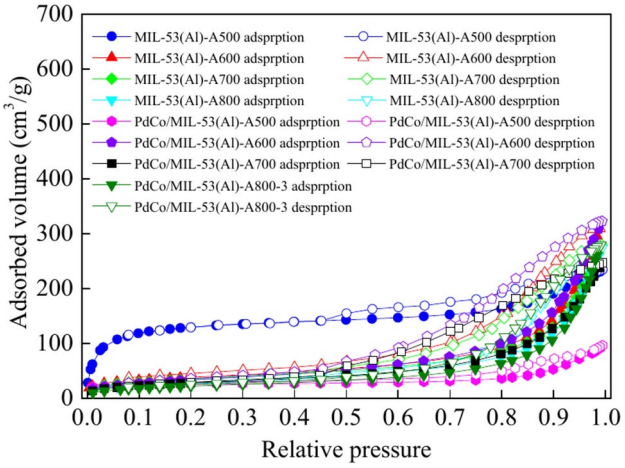

Fig. 2. N_2 adsorption–desorption isotherms of the samples.

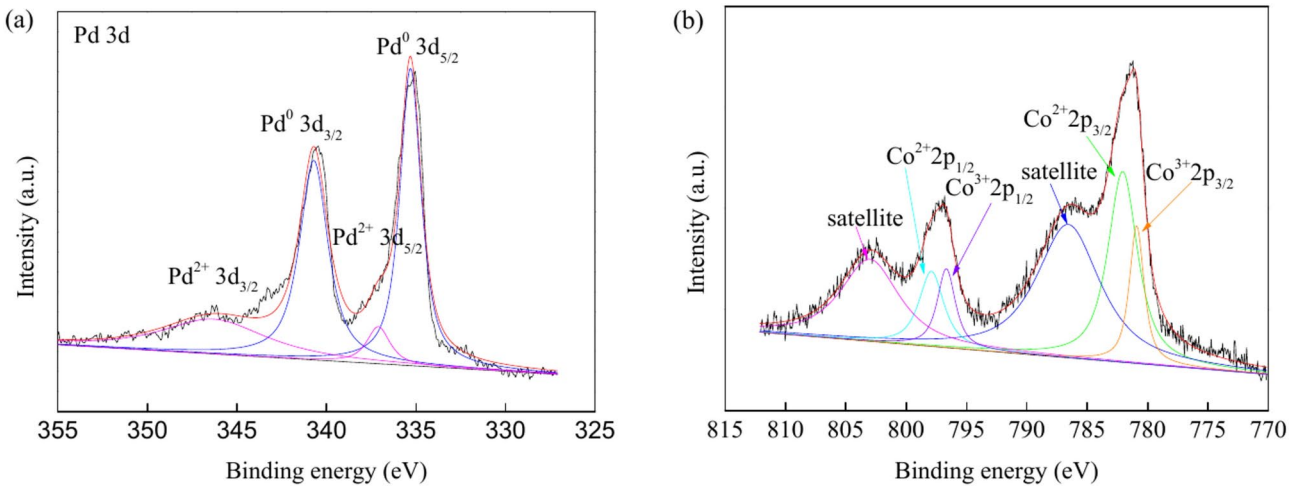

Fig. 3. XPS spectra of Pd 3d (**a**) and Co 2p (**b**) in the PdCo/MIL-53(Al)-A700 catalyst.

The presence of Co changed the electronic structure of the Pd^0 particles, resulting in an increased binding energy of Pd^0[27]. Additionally, the Co 2p spectra of PdCo/MIL-53(Al)-A700 revealed four main peaks at 797.9, 782.1, 796.7 and 780.9 eV, corresponding to the binding energies of Co^{2+} $2p_{1/2}$, Co^{2+} $2p_{3/2}$, Co^{3+} $2p_{1/2}$ and Co^{3+} $2p_{3/2}$, respectively (Fig. 3b)[75–77]. Two additional peaks at 803.0 and 786.6 eV in the deconvoluted Co 2p XPS spectra were assigned to the satellite features of Co $2p_{1/2}$ and Co $2p_{3/2}$ (Fig. 3b)[78]. Analysis of the Co 2p XPS for PdCo/MIL-53(Al)-A700 confirmed the presence of both Co^{2+} and Co^{3+} species. The proportion of surface cobalt species was estimated by evaluating the peak area ratio, revealing a molar ratio of Co^{2+}:Co^{3+} of 2.2:1.

The representative TEM images and size distributions of Pd–Co nanoparticles for PdCo/MIL-53(Al)-A500, PdCo/MIL-53(Al)-A600, PdCo/MIL-53(Al)-A700 and PdCo/MIL-53(Al)-A800-3 are shown in Fig. 4. The Pd–Co nanoparticles across all catalysts displayed a nearly spherical in morphology and were uniformly distributed on the support surface. The average sizes of the Pd–Co nanoparticles were 9.4, 10.9, 8.5 and 12.4 nm for PdCo/MIL-53(Al)-A500, PdCo/MIL-53(Al)-A600, PdCo/MIL-53(Al)-A700 and PdCo/MIL-53(Al)-A800-3, respectively. The average sizes of the Pd–Co nanoparticles varied as follows: PdCo/MIL-53(Al)-A700 < PdCo/MIL-53(Al)-A500 < PdCo/MIL-53(Al)-A600 < PdCo/MIL-53(Al)-A800-3. For the Pd/MIL-53(Al)-A700 catalyst, the Pd nanoparticles ranged in size from 2 to 14 nm, with an average diameter of 7.0 nm (Fig. S4). The element distribution in PdCo/MIL-53(Al)-A700 was further analysed using HAADF–STEM and EDS, which showed that Pd and Co were well mixed and uniformly distributed on the support (Fig. 5). This analysis confirmed the formation of Pd–Co alloys in the PdCo/MIL-53(Al)-A700 catalyst.

Catalytic performance for 1,3-butadiene hydrogenation

The catalytic performance for the selective hydrogenation of 1,3-butadiene on various bimetallic Pd–Co catalysts was evaluated in a fixed-bed flow reactor under atmospheric pressure, with reaction temperature ranging from 20 to 40 °C. Initially, the catalytic performance of PdCo/MIL-53(Al)-A800-3 was studied to gain insights into the effects of reaction temperature, Pd and Co contents and space velocity. Figure 6a–d illustrate the evolution of 1,3-butadiene conversion and product selectivity for the hydrogenation on PdCo/MIL-53(Al)-A800-3 at temperatures of 20 °C, 30 °C and 40 °C over time. The catalytic activity of the blank (without catalyst) was negligible with a 1,3-butadiene conversion of less than < 1% at temperatures ranging from 20 to 40 °C. The reaction temperature considerably affected the conversion of 1,3-butadiene and product selectivity over the PdCo/MIL-53(Al)-A800-3 catalyst during the hydrogenation reaction. As illustrated in Fig. 6a, increasing the reaction temperature led to a rise in 1,3-butadiene conversion. At 20 °C, the initial conversion was 82.9%, which then decreased to 18.6% after 2.5 h of operation, with the conversion remaining stable from 2.5 to 6 h. At 30 °C, the conversion started at 99.9% and gradually declined to 77.8% over a period of 6 h. At a reaction temperature of 40 °C, the initial 1,3-butadiene conversion was 99.7%, and this high conversion remained stable for up to 2.5 h. Afterwards, the conversion gradually decreased from 99.5 to 78.2% over the next 2 h. The primary product of the 1,3-butadiene hydrogenation was butenes (including 1-butene, *trans*-2-butene, and *cis*-2-butene), while butane, a byproduct formed from the further hydrogenation of butenes, was also produced. The selectivity for total butenes increased with time on stream for the PdCo/MIL-53(Al)-A800-3 catalyst at 20 °C. The selectivity for total butenes reached 78.3% in 3 h, and then stabilised from 3.0 to 6 h as the reaction progressed. At 20 °C, the distribution of different butenes was as follows: 1-butene (25.0–42.6%) > *trans*-2-butene (13.8–31.3%) > *cis*-2-butene (5.4–8.6%) at all reaction time. The selectivity for butane decreased from 55.8 to 21.6% over the first 3.5 h at 20 °C, remaining relatively constant from 3.5 to 6 h. When the reaction temperature was rised to 30 °C, the selectivity for total butenes increased from 21.3 to 75.6% with extended time on stream. However, the selectivity for butane decreased from 78.7 to 24.4% as the reaction time increased. The selectivity for different butene isomers was ranked as follows: *trans*-2-butene (14.1–38.9%) > 1-butene (2.0–22.4%) > *cis*-2-butene (5.2–14.4%). At 40 °C, the selectivity for total butenes initially decreased slightly from 42.5 to 41.3% during the first 0.25 h of the reaction, then increased from 41.3 to 55.6% as the reaction time increased from 0.25 to 4 h. This selectivity

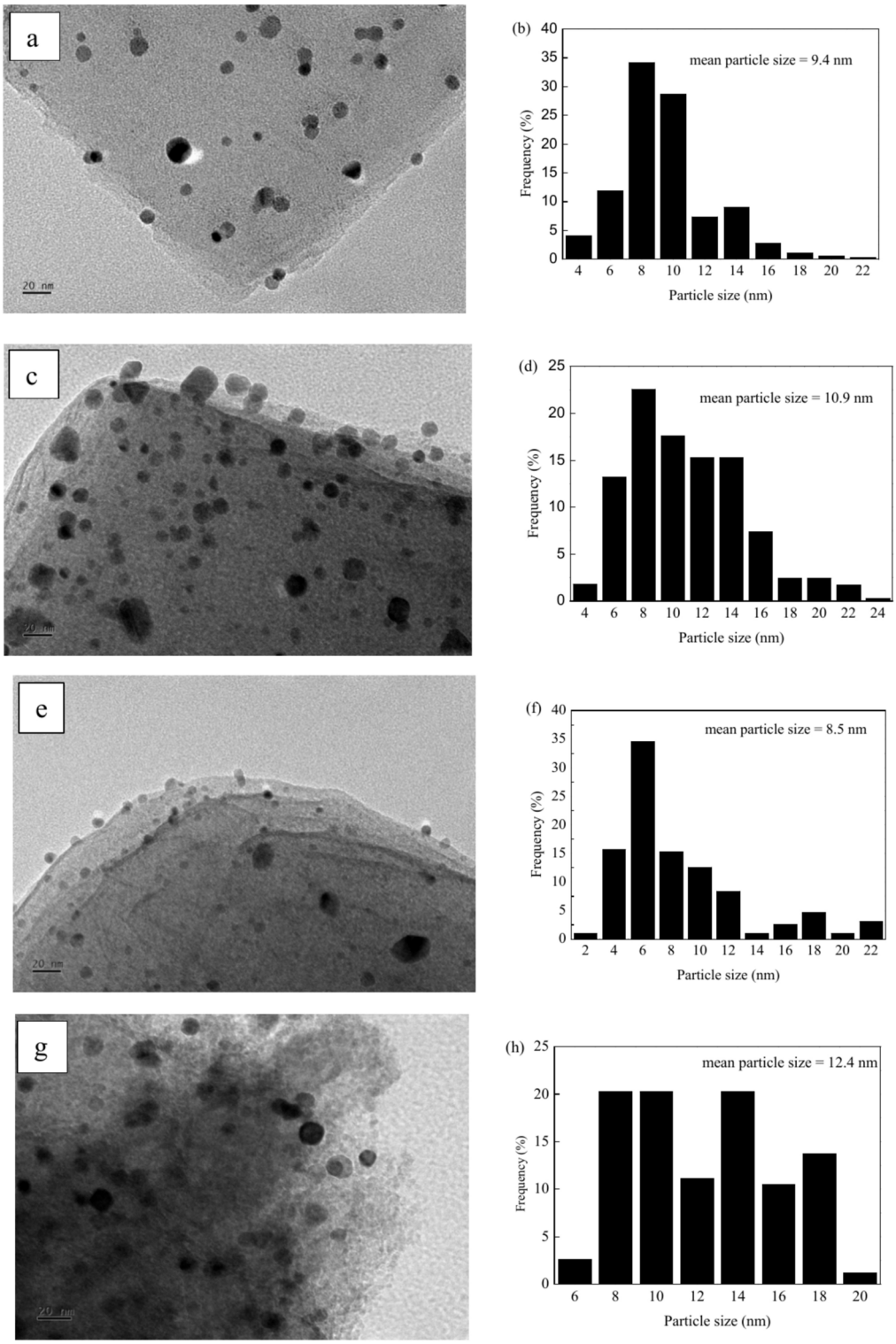

Fig. 4. TEM images and PdCo nanoparticle size distributions of PdCo/MIL-53(Al)-A500 (**a**,**b**), PdCo/MIL-53(Al)-A600 (**c**,**d**), PdCo/MIL-53(Al)-A700 (**e**,**f**) and PdCo/MIL-53(Al)-A800-3 (**g**,**h**).

remained relatively stable from 4 to 6 h. In contrast, the selectivity for butane followed the opposite trend, varying between 44.4 and 58.7%. The selectivity for 1-butene first decreased during the first 0.25 h of the reaction, then increased slightly as the reaction progressed from 0.25 to 3.5 h, with values ranging from 4.6 to 21.6%. It remained relatively constant from 3.5 to 6 h. The selectivity for *trans*-2-butene and *cis*-2-butene varied from 22.6% to 27.5% and from 6.8 to 10.5%, respectively, during the reaction period. Figure 6e illustrates the product selectivity for PdCo/MIL-53(Al)-A800-3 at 90% conversion of 1,3-butadiene across temperatures of 20 °C, 30 °C and 40 °C.

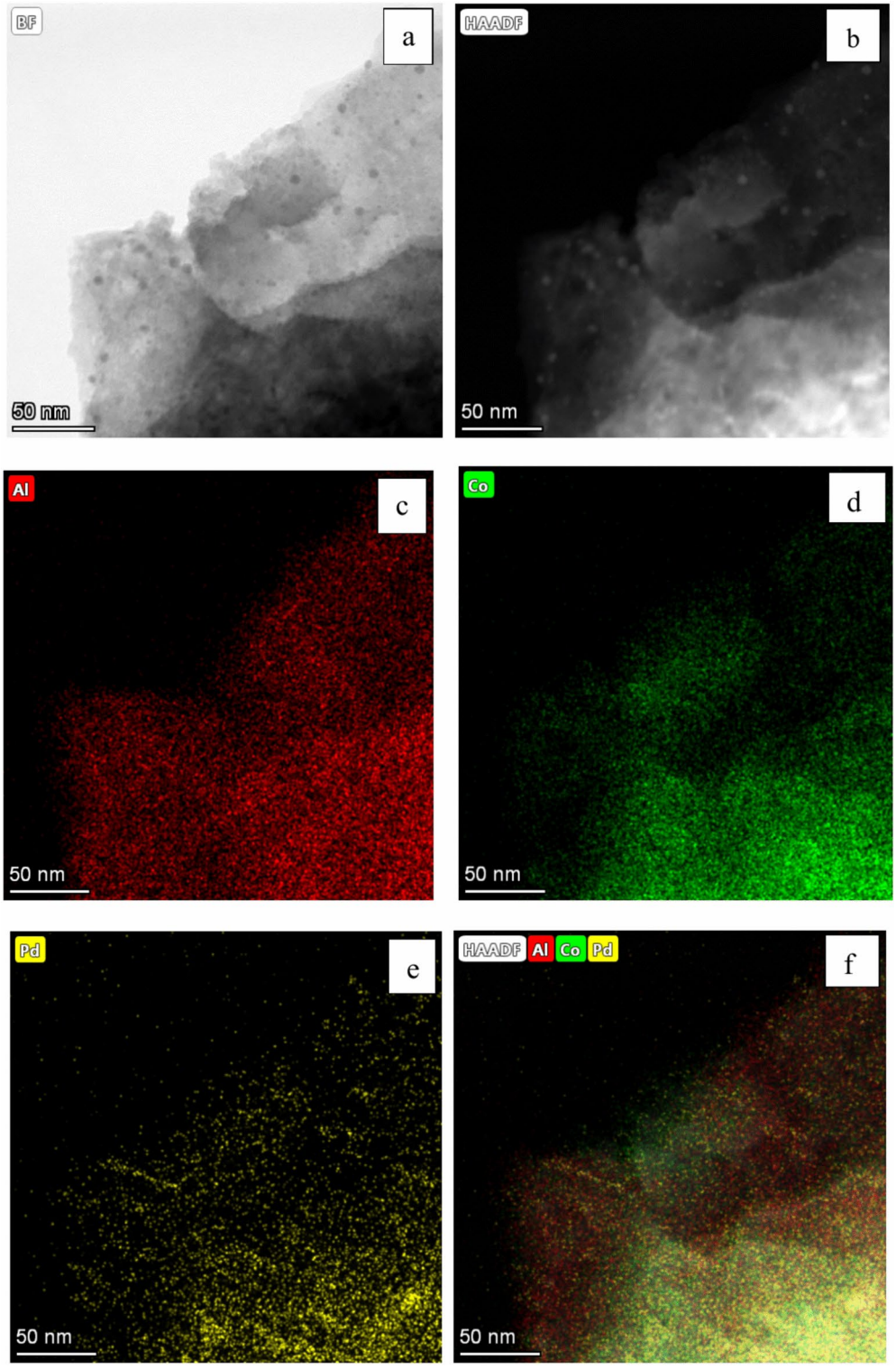

Fig. 5. TEM image (**a**), HAADF-STEM image (**b**), and EDS elemental mapping images (**c**–**f**) of PdCo/MIL-53(Al)-A700.

The selectivities for total butenes were 41.2%, 44.2% and 53.4% at 90% conversion on PdCo/MIL-53(Al)-A800-3 catalyst at 20 °C, 30 °C and 40 °C, respectively (Fig. 6e). The selectivity for total butenes increased with the increase of reaction temperature at 90% 1,3-butadiene conversion, indicating that high reaction temperature improved the selectivity of total butenes. This phenomenon may be due to the stronger adsorption of 1,3-butadiene on surface of Pd–Co nanoparticles at high temperature[79]. Moreover, the selectivity for 1-butene, *trans*-2-butene and *cis*-2-butene were similar on PdCo/MIL-53(Al)-A700 catalyst at low temperature (20 °C and 30 °C), suggesting

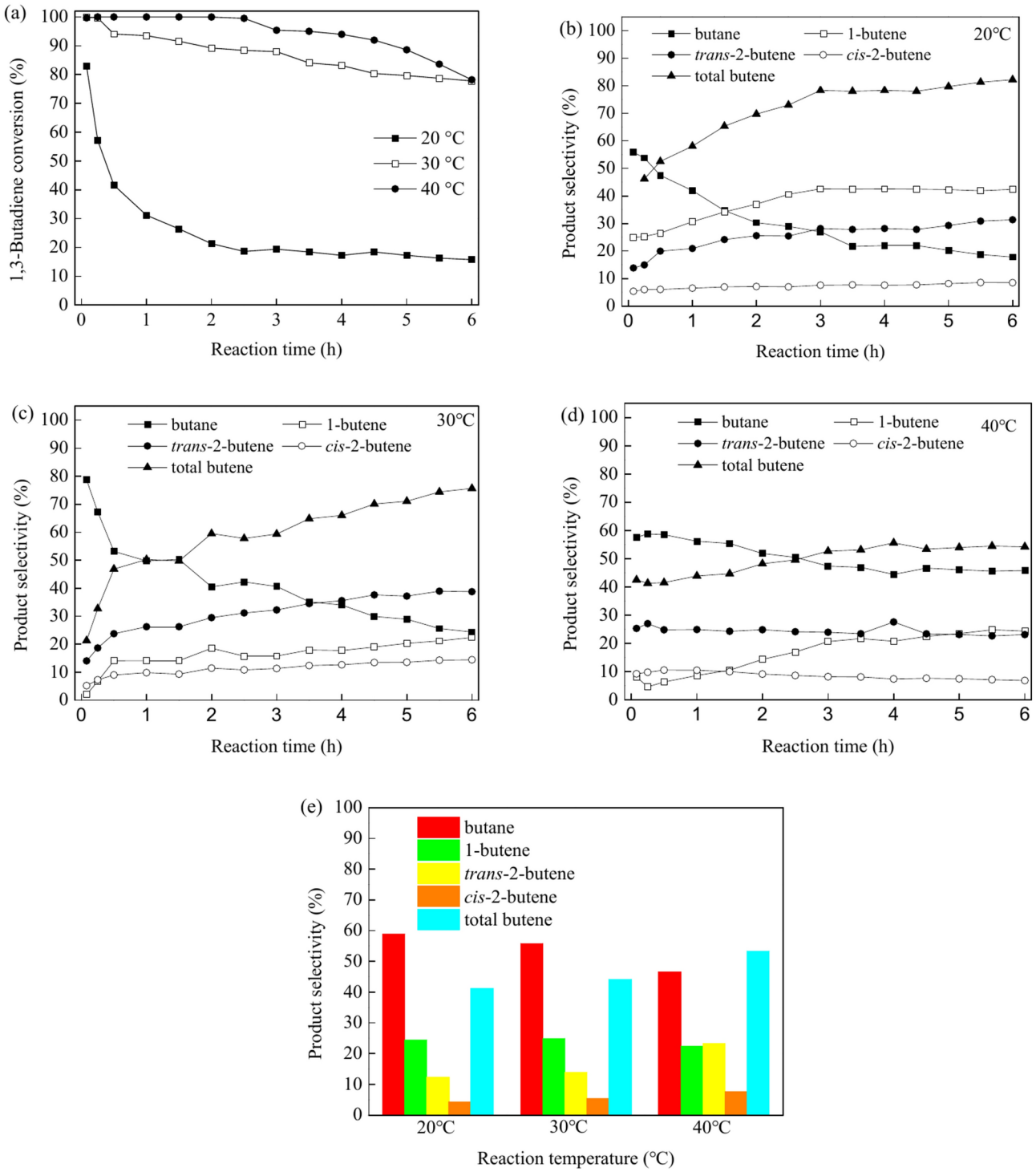

Fig. 6. Evolution of the 1,3-butadiene conversion (**a**), product selectivity (**b**–**d**) for 1,3-butadiene hydrogenation on PdCo/MIL-53(Al)-A800-3 at 20 °C (**b**), 30 °C (**c**) and 40 °C (**d**) as a function of reaction time, and product selectivity on PdCo/MIL-53(Al)-A800-3 at 90% conversion of 1,3-butadiene (**e**) (reaction conditions: 5 mg of catalyst, 20.0 mL/min of 1,3-butadiene/N_2, 10 mL/min of H_2).

that no isomerization was detected during 1,3-butadiene hydrogenation at low temperature[56,80]. However, the selectivities for *trans*-2-butene and cis-2-butene was increased at high reaction temperature of 40 °C, while that of 1-butene decreased, suggesting that 1-butene isomerized to *tr*ans-2-butene and *cis*-2-butene at high reaction temperature[26,56]. As shown the results above, PdCo/MIL-53(Al)-A800-3 demonstrated excellent 1,3-butadiene conversion and good total butene selectivity at 40 °C.

Figure S5 illustrates the evolution of 1,3-butadiene conversion and TOF over time and product selectivity at 90% 1,3-butadiene conversion during the hydrogenation process on PdCo/MIL-53(Al)-A800 with varying Pd and Co contents. The Pd and Co contents considerably influenced both the conversion of 1,3-butadiene and the product selectivity. Specifically, the 1,3-butadiene conversion increased with higher Pd and Co contents (Fig. S5a). However, the turnover frequency (TOF) based on the total metal content (Pd and Co) decreased as the Pd and Co contents increased (Fig. S5b). For instance, the conversions of 1,3-butadiene at 40 °C in 2 h were 50.2%, 78.5% and 100% for PdCo/MIL-53(Al)-A800-1, PdCo/MIL-53(Al)-A800-2 and PdCo/MIL-53(Al)-A800-3, respectively. The calculated TOFs based on total metal content were 217.7, 131.9 and 98.1 h^{-1} for PdCo/MIL-53(Al)-A800-1, PdCo/MIL-53(Al)-A800-2 and PdCo/MIL-53(Al)-A800-3, respectively. PdCo/MIL-53(Al)-A800-1 catalyst exhibited the highest catalytic activity for 1,3-butadiene hydrogenation. The reduced Pd and Co contents might enhance nanoparticle dispersion, ensuring adequate exposure of Pd–Co nanoparticles to the raw material of 1,3-butadiene hydrogenation[81]. The selectivities for 1-butene, *trans*-2-butene and *cis*-2-butene were 52.8%, 27.9% and 13.2% at 90% conversion on PdCo/MIL-53(Al)-A800-1 catalyst, respectively (Fig. S5c). PdCo/MIL-53(Al)-A800-2 and PdCo/MIL-53(Al)-A800-3 displayed similar selectivities for 1-butene (22.4% and 22.4%), *trans*-2-butene (20.4% and 23.4%) and *cis*-2-butene (7.5% and 7.6%) at 90% 1,3-butadiene conversion (Fig. S5c). The selectivities for total butenes were 94.1%, 50.2% and 53.4% on PdCo/MIL-53(Al)-A800-1, PdCo/MIL-53(Al)-A800-2 and PdCo/MIL-53(Al)-A800-3 catalysts at 90% 1,3-butadiene conversion, respectively, indicating that the low Pd and Co contents could inhibit the secondary hydrogenation of butenes to butane (Fig. S5c).

Figure S6 shows the impact of space velocity on the conversion of 1,3-butadiene, TOF and product selectivity for the selective hydrogenation of 1,3-butadiene using the PdCo/MIL-53(Al)-A800-3 catalyst. The conversion of 1,3-butadiene decreased with rising space velocity from 0.5 to 6 h (Fig. S6a). However, during the initial 0.25–0.5 h, the conversion values followed the order: 360 L/(h·g_{cat}) > 900 L/(h·g_{cat}) > 600 L/(h·g_{cat}) (Fig. S6a). The PdCo/MIL-53(Al)-A800-3 catalyst exhibited the highest TOF values at a space velocity of 900 L/(h·g_{cat}) during all reaction times (Fig. S6b). For the first 1.5 h of the reaction, the TOF values were higher at 600 L/(h·g_{cat}) than at 360 L/(h·g_{cat}) (Fig. S6b). However, from 1.5 to 6 h, the TOF values were higher at 360 L/(h·g_{cat}) than at 600 L/(h·g_{cat}) (Fig. S6b). The selectivity for total butenes increased as space velocity increased at 90% conversion (Fig. S5f.). The total butene selectvities were 53.4%, 57.5% and 60.0% with space velocity of 360, 600 and 900 L/(h·g_{cat}), respectively, on PdCo/MIL-53(Al)-800–3 catalyst at 90% conversion (Fig. S6f.). However, the selectivities for 1-butene, *trans*-2-butene and *cis*-2-butene did not apparently variation with different space velocity, indicating that no isomerization was detected during 1,3-butadiene hydrogenation[56,80].

The effect of pyrolysis temperature on the conversion of 1,3-butadiene and product selectivity for its hydrogenation was investigated, and the results are shown in Fig. 7. The PdCo/MIL-53(Al)-A700 catalyst exhibited the highest 1,3-butadiene conversion, with approximately 100% 1,3-butadiene conversion at all reaction times (Fig. 7a). The PdCo/MIL-53(Al)-A600 and PdCo/MIL-53(Al)-A800-3 catalysts showed similar 1,3-butadiene conversion during the first 2 h, but the conversion decreased with increased time on stream from 2.5 to 6 h (Fig. 7a). At 40 °C over 6 h, the conversions of 1,3-butadiene were 87.4% for PdCo/MIL-53(Al)-A600 and 78.2% for PdCo/MIL-53(Al)-A800-3 (Fig. 7a). PdCo/MIL-53(Al)-A500 exhibited the lowest conversion of 1,3-butadiene, ranging from 23 to 33% at 40 °C (Fig. 7a). The TOF based on the total metal content (Pd and Co) presented similar shaped with 1,3-butadiene conversion as a function of time for PdCo/MIL-53(Al)-A500, PdCo/MIL-53(Al)-A600, PdCo/MIL-53(Al)-A700 and PdCo/MIL-53(Al)-A800-3 catalysts (Fig. 7b). PdCo/MIL-53(Al)-A700 catalyst exhibited the highest TOF of 103.5 h^{-1} from initial time to 6 h. The support type and nanoparticle size play a significant role in the catalytic activity for the hydrogenation of 1,3-butadiene[31,82]. The XRD exhibited that MIL-53(Al) retained its original structure after pyrolysis at 500℃ but fully decomposed into Al_2O_3 after pyrolysis at 600 °C–800℃ (Fig. 1). The average sizes of the Pd–Co nanoparticles were 9.4, 10.9, 8.5, and 12.4 nm for PdCo/MIL-53(Al)-A500, PdCo/MIL-53(Al)-A600, PdCo/MIL-53(Al)-A700 and PdCo/MIL-53(Al)-A800-3, respectively (Fig. 4). The PdCo/MIL-53(Al)-A700 catalyst, with an average Pd–Co nanoparticle size of 8.5 nm, demonstrated superior 1,3-butadiene conversion in 1,3-butadiene hydrogenation, attributing to the type of support (Al_2O_3) and reduced size of the Pd–Co nanoparticles[83]. As shown in Fig. 7c, the selectivity for total butenes remained relatively constant throughout the reaction time for the PdCo/MIL-53(Al)-A500 catalyst, with values ranging from 74.9% to 76.9%. The distributions of different products followed the order of 1-butene (39.1%–46.4%) > *trans*-2-butene (22.5–27.9%) ≈ butane (23.7–25.6%) > *cis*-2-butene (6.6%–8.1%) from initial time to 6 h (Fig. 7c). For the PdCo/MIL-53(Al)-A500 catalyst, 1-butene was the predominant product at all reaction time. In contrast, for the PdCo/MIL-53(Al)-A600 catalyst, the selectivity for total butenes increased from 20.5% to 65.5% as time on stream progressed (Fig. 7d). Concurrently, the selectivity for butane decreased from 79.5% to 34.5% with increasing reaction time (Fig. 7d). Selectivities for 1-butene, *trans*-2-butene and *cis*-2-butene also increased with longer reaction times. The distribution of different butenes followed the order of *trans*-2-butene (12.5%–29.2%) > 1-butene (3.3%–24.7%) > *cis*-2-butene (5.0%–14.6%) from initial time to 6 h (Fig. 7d). For the PdCo/MIL-53(Al)-A700 catalyst, selectivity for total butenes increased from 22.7% to 62.6% as the time on stream progressed (Fig. 7e). Concurrently, the selectivity for butane decreased from 77.3% to 37.4% with increasing reaction time (Fig. 7e). The selectivity for 1-butene increased slightly over time, with values ranging from 6.9% to 29.4% (Fig. 7e). The selectivity for *trans*-2-butene increased from 10.1% to 22.3% during the first 1 h, then decreased from 1 to 3 h, and stabilised at approximately 15% from 3.0 to 6.0 h over PdCo/MIL-53(Al)-A700 at 40 °C (Fig. 7e). The selectivity for *cis*-2-butene also increased slightly with longer reaction times, ranging from 5.8% to 17.4% (Fig. 7e). For PdCo/MIL-53(Al)-A800-3 catalyst, the selectivity for total butenes initially decreased slightly from 42.5% to 41.3% during the first 0.25 h of the reaction, then increased from 41.3% to 55.6% as the time on stream extended from 0.25 to 4 h, and remained relatively constant from 4 to 6 h (Fig. 7f). The percentages of different products followed the order of butane (44.4%–58.7%) > *trans*-2-butene (22.6%–27.0%) > 1-butene (4.6%–24.8%) > *cis*-2-butene (6.8%–10.5%) at all reaction time (Fig. 7f). Specially,

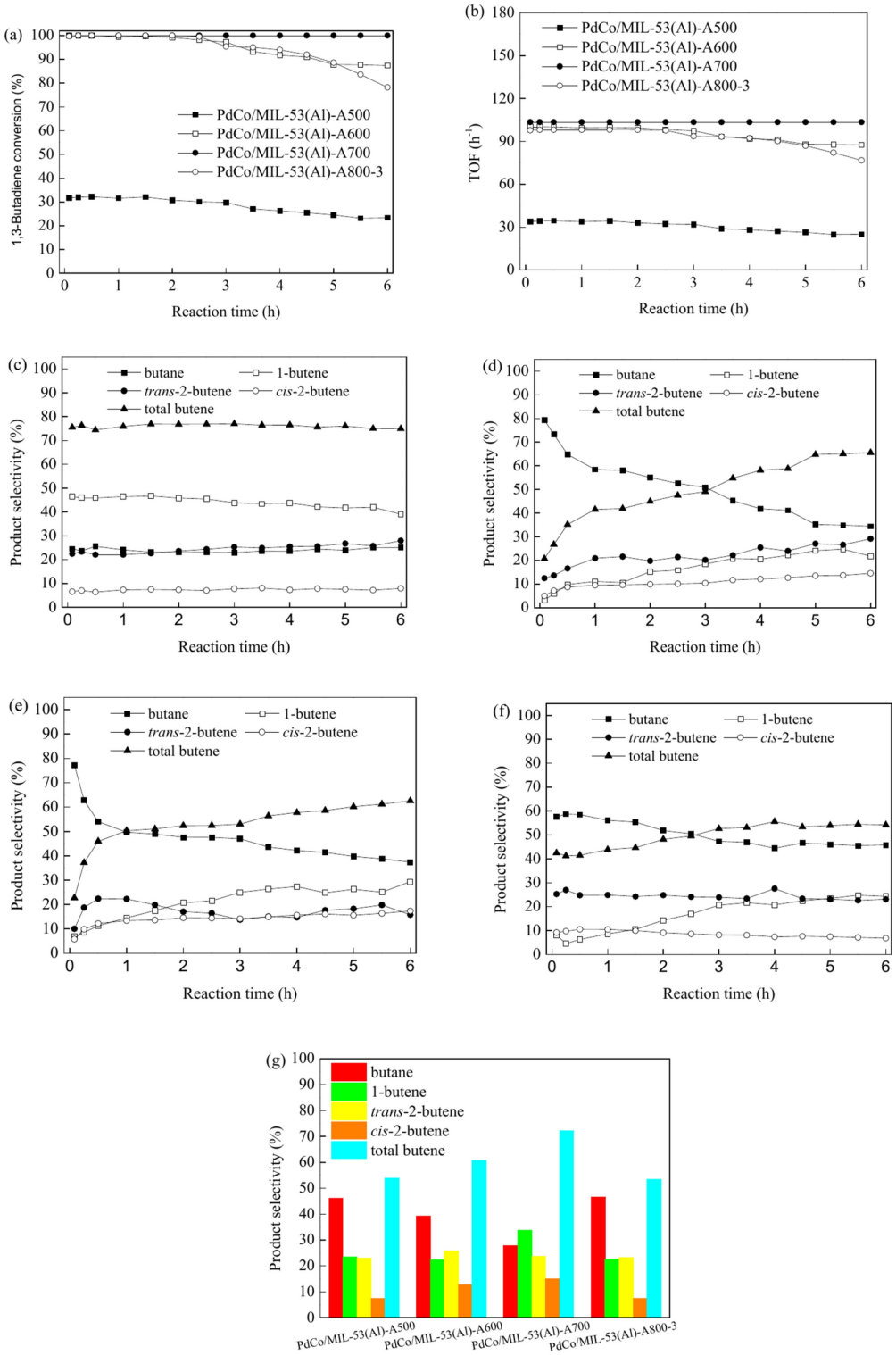

Fig. 7. Evolution of the conversion of 1,3-butadiene (**a**), TOF (**b**), product selectivity (**c**–**f**) for hydrogenation of 1,3-butadiene on PdCo/MIL-53(Al)-A500 (**c**), PdCo/MIL-53(Al)-A600 (**d**), PdCo/MIL-53(Al)-A700 (**e**), and PdCo/MIL-53(Al)-A800-3 (**f**) as a function of reaction time, and product selectivity at 90% 1,3-butadiene conversion (**g**) (reaction conditions: 5 mg of catalyst, 20.0 mL/min of 1,3-butadiene/N_2, 10 mL/min of H_2, 40 °C).

the selectivities for total butenes were 54.0%, 60.8%, 72.3% and 53.4% on PdCo/MIL-53(Al)-A500, PdCo/MIL-53(Al)-A600, PdCo/MIL-53(Al)-A700 and PdCo/MIL-53(Al)-A800-3 at 90% conversion, respectively (Fig. 7g). The PdCo/MIL-53(Al)-A700 catalyst exhibited highest selectivity for total butenes at 90% conversion of 1,3-butadiene. As shown the results above, the PdCo/MIL-53(Al)-A700 catalyst presented the best 1,3-butadiene conversion and total butene selectivity.

To elucidate the effect of Pd–Co alloying on the catalytic performance of Pd in the selective hydrogenation of 1,3-butadiene, the performance of the PdCo/MIL-53(Al)-A700 and Pd/MIL-53(Al)-A700 catalysts was compared (Fig. 8). For the monometallic catalyst Pd/MIL-53(Al)-A700, the 1,3-butadiene conversion was nearly 99% during the first 0.25 h but then rapidly declined to 40.3% at 6 h (Fig. 8a). In contrast, the bimetallic PdCo/MIL-53(Al)-A700 catalyst demonstrated consistently high activity, achieving 100% conversion of 1,3-butadiene throughout the reaction time (Fig. 8a). After introducing Co elements into the catalyst for PdCo/MIL-53(Al)-A700, the 1,3-butadiene conversion was initially similar to that of monometallic Pd/MIL-53(Al)-A700 during the first 0.5 h of reaction time. However, from 0.5 to 6 h, it was significantly higher than that of monometallic Pd/MIL-53(Al)-A700. The results indicated that the bimetallic PdCo/MIL-53(Al)-A700 catalyst exhibited better stability than monometallic Pd/MIL-53(Al)-A700. The enhanced stability for PdCo/MIL-53(Al)-A700 catalyst can be attributed to the synergistic effects between Pd and Co[83,84]. The selectivity of total butenes over the Pd/MIL-53(Al)-A700 catalyst rapidly increased to 64.0% within the first 1 h and then gradually increased to 80.0% over the next 5 h (Fig. 8b). The selectivity toward total butenes over the PdCo/MIL-53(Al)-A700 catalyst rapidly increased from 22.7% intially to 45.9% at 0.5 h, followed by a gradual increase to 62.6% at 6 h (Fig. 8b). The selectivity of total butenes for the PdCo/MIL-53(Al)-A700 catalyst was higher than that of the monometallic Pd/MIL-53(Al)-A700 catalyst at similar 1,3-butadiene conversions (> 99.0%). However, the total butene selectivity of the bimetallic PdCo/MIL-53(Al)-A700 catalyst was lower than that of the monometallic Pd/MIL-53(Al)-A700 from 1 to 6 h, even though the 1,3-butadiene conversion was higher with the PdCo/MIL-53(Al)-A700 catalyst. Overall, the bimetallic PdCo/MIL-53(Al)-A700 catalyst exhibited better 1,3-butadiene conversion and total butene selectivity at similar 1,3-butadiene conversion (> 99.0%) compared to the monometallic Pd/MIL-53(Al)-A700 catalyst. This improvement is likely due to the synergistic interactions of the Pd–Co alloy nanoparticles in the PdCo/MIL-53(Al)-A700 catalyst[56,85–88].

The stability and regeneration capabilities are crucial parameters for catalysts in industrial applications[89]. The stability and regeneration of the PdCo/MIL-53(Al)-A700 catalyst were assessed at 40 °C. Figure 9 illustrates the evolution of 1,3-butadiene conversion and total butene selectivity over time for both fresh and regenerated PdCo/MIL-53(Al)-A700 catalysts. The 1,3-butadiene conversion for the fresh PdCo/MIL-53(Al)-A700 catalyst remained constant at 100% for the first 6 h but showed signs of deactivation with prolonged time on stream (Fig. 9a). After 147 h, the 1,3-butadiene conversion decreased from 100% to 53.0% (Fig. 9a). The selectivity toward total butenes increased rapidly with time on stream during the first 40 h of reaction and then continued to rise gradually increased from 40 to 147 h (Fig. 9b). The fresh PdCo/MIL-53(Al)-A700 catalyst initially exhibited a total butene selectivity of 22.7%, which increased to 87.1% after 147 h (Fig. 9b). Spent PdCo/MIL-53(Al)-A700 catalyst exhibited the similar PXRD patterns with fresh PdCo/MIL-53(Al)-A700 catalyst (Fig. 10a). The peak at $2\theta = 26.7°$ are characteristic of θ-Al_2O_3, while the peaks at $2\theta = 40.1°$, 45.7° and 67.2° attributed to γ-Al_2O_3[58–61]. The TEM image and Pd–Co nanoparticle size distribution of spent PdCo/MIL-53(Al)-A700 catalyst are shown in Figs. 10d and e. There was no greatly aggregation of Pd–Co nanoparticles for spent PdCo/MIL-53(Al)-A700 because of the stabilizing effect of Al_2O_3 and synergistic effect between Pd and Co[36]. The mean paricle size of Pd–Co nanoparticles for the spent PdCo/MIL-53(Al)-A700 catalyst was 8.9 nm. The mean Pd–Co nanoparticle size of fresh PdCo/MIL-53(Al)-A700 catalyst was 8.5 nm (Fig. 4). Only 4.7% of mean Pd–Co nanoparticle size was increased due to the highly dispersion of Pd–Co nanoparticles and synergistic effect of Pd and Co, which had

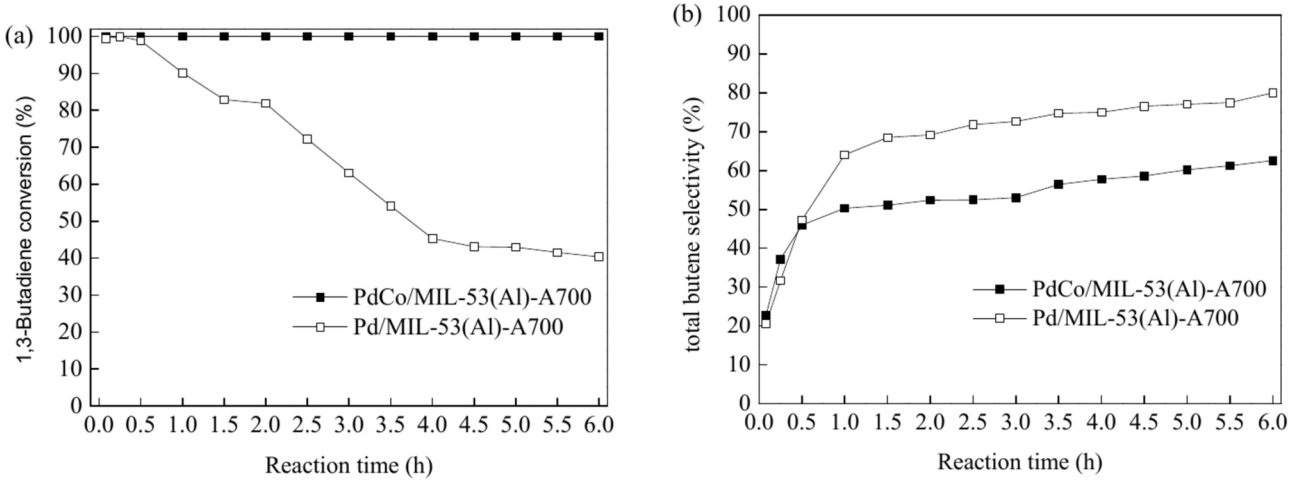

Fig. 8. Evolution of the conversion of 1,3-butadiene (**a**), and total butene selectivity (**b**) for the hydrogenation of 1,3-butadiene on PdCo/MIL-53(Al)-A700, and Pd/MIL-53(Al)-A700 as a function of reaction time (reaction conditions: 5 mg of catalyst, 20.0 mL/min of 1,3-butadiene/N_2, 10 mL/min of H_2, 40 °C).

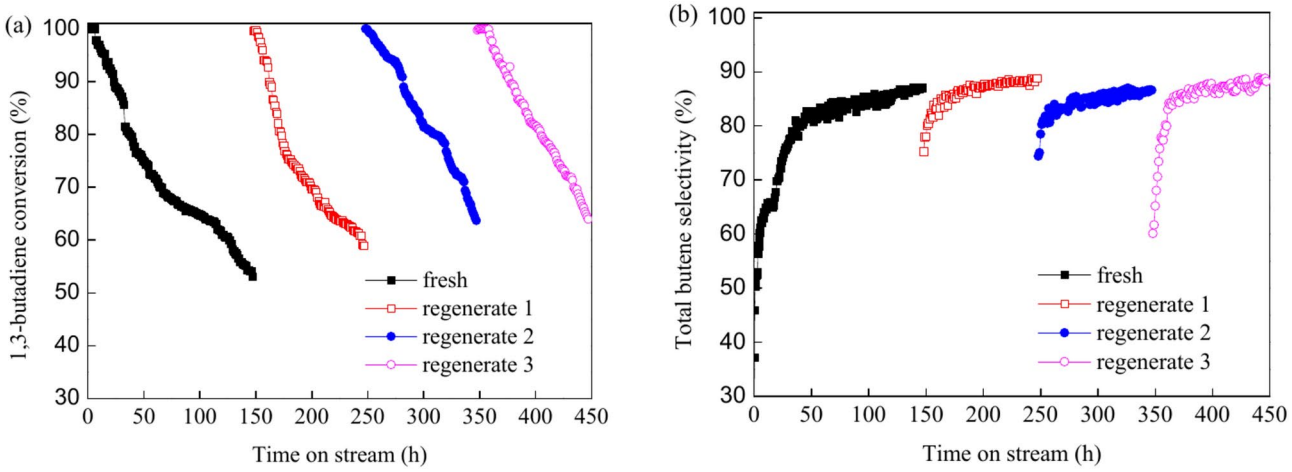

Fig. 9. The stability test of the fresh PdCo/MIL-53(Al)-A700 and regeneration of the PdCo/MIL-53(Al)-A700 catalyst for hydrogenation of 1,3-butadiene (reaction conditions: 5 mg of catalyst, 20 mL/min of 1,3-butadiene/N_2, 10 mL/min of H_2, 40 °C of reaction temperature).

little effect on deactivation during 147 h on stream. The Raman spectra of spent PdCo/MIL-53(Al)-A700 catalyst exhibited two peaks at 1352 cm^{-1} (D band) and 1582 cm^{-1} (G band) which can be correspond to the amorphous carbon species and filamentous/graphitic carbon species, respectively (Fig. 10b)[27]. As shown in Fig. 10c, the distinct weight loss (6.5%) from 30 to 391 °C was attributed to the desorption of physically adsorbed raw and product materials. The TG curve of spent PdCo/MIL-53(Al)-A700 exhibited a slight increase (0.1%) in weight from 391 °C to 421 °C, corresponding to the oxidation of Pd^0 to Pd^{2+}[27]. The carbon deposits were oxidized at 421–903 °C, which were consistent with the literature[90]. The weight loss (2.0%) from 421 to 840 °C corresponded to the amorphous carbon deposits, while the weight loss (0.7%) in the range from 840 °C to 903 °C ascribed to the filamentous/graphitic carbon deposits[91]. Raman and TG characterization results revealed that the carbon can be deposited on the PdCo/MIL-53(Al)-A700 during 1,3-butadiene hydrogenation. Previous studies have shown that carbon deposited on catalysts during 1,3-butadiene hydrogenation can block catalyst pores or cover active sites[27,69]. This carbon buildup often results in reduced hydrogenation activity. Therefore, the degradation for PdCo/MIL-53(Al)-A700 was mainly ascribed to the carbon deposition on the catalyst. The spent PdCo/MIL-53(Al)-A700 catalyst was regenerated three times by exposing it to a flow of N_2 (20 mL/min) at 200 °C for 2 h to remove the carbon deposits. After three regeneration cycles, the PdCo/MIL-53(Al)-A700 catalyst showed a similar 1,3-butadiene conversion and total butene selectivity profiles to those of the fresh catalyst. This indicates that PdCo/MIL-53(Al)-A700 can be effectively regenerated three times under these conditions.

Conclusion

In conclusion, a series of bimetallic Pd–Co catalysts supported on Al_2O_3 derived from MIL-53(Al) at various calcination temperatures were successfully synthesised using the co-impregnation method. The catalytic performance of these bimetallic Pd–Co catalysts was evaluated in the selective hydrogenation of 1,3-butadiene at low temperatures between 20 and 40 °C, with 10 °C intervals and at atmospheric pressure. The PdCo/MIL-53(Al)-A700 catalyst exhibited a strong synergistic effect during 1,3-butadiene hydrogenation, delivering considerably higher 1,3-butadiene conversion and total butene selectivity compared to the monometallic Pd/MIL-53(Al)-A700 catalyst, demonstrating its potential for application on an industrial scale. In addition, the PdCo/MIL-53(Al)-A700 catalyst can be readily regenerated three times in an N_2 flow at 200 °C, with no noticeable loss in catalytic activity or total butene selectivity. The findings presented here may pave the way for the development of low-cost, high-performance, and stable heterogeneous bimetallic catalysts by introducing non-precious metals into noble metal catalysts using MOF-derived supports. We believe that MOF-derived supported bimetallic nanoparticle catalysts will play a significant role in diverse applications moving forward.

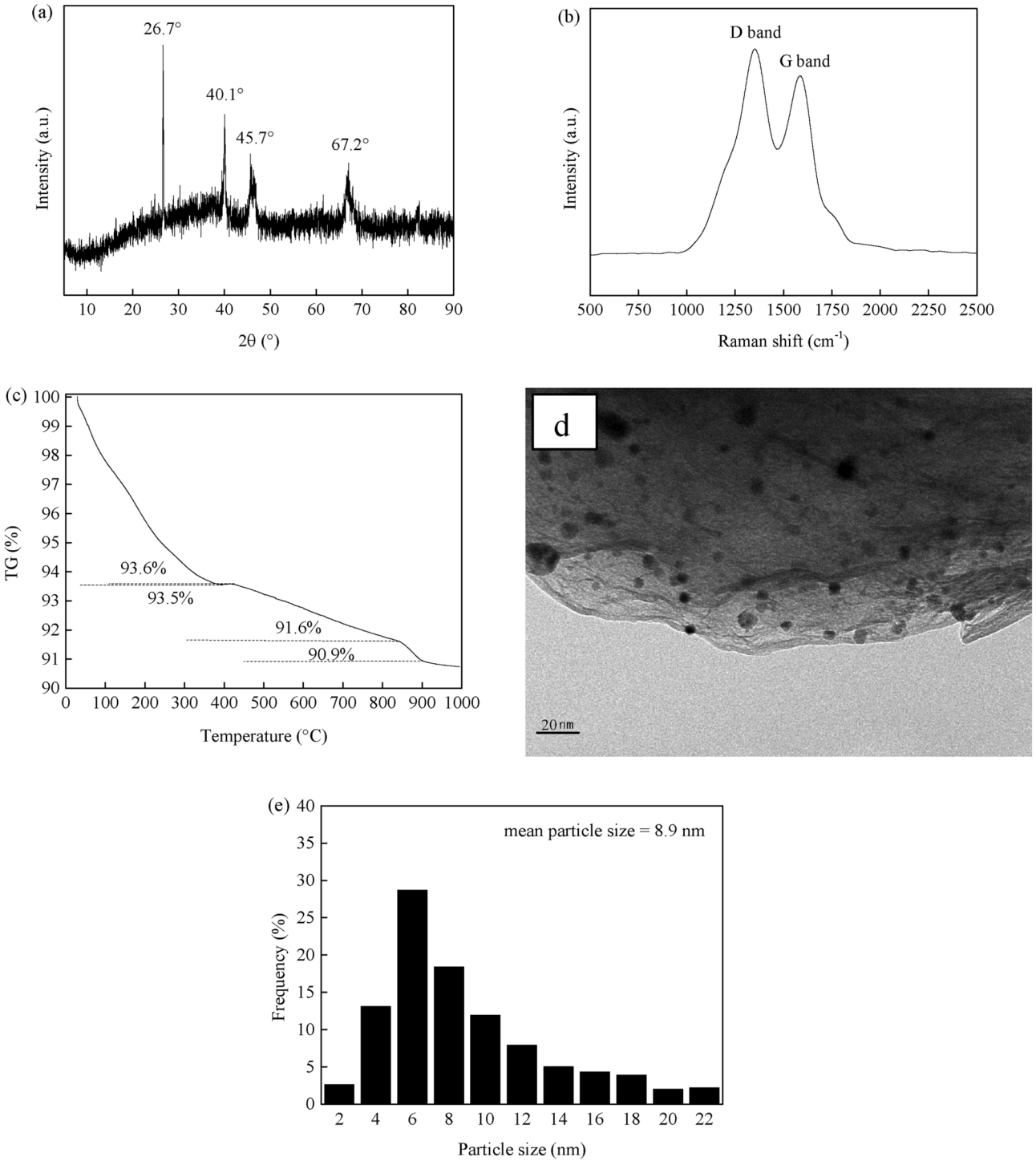

Fig. 10. The PXRD pattern (**a**), Raman spectra (**b**), TG curve (**c**), TEM image (**d**), and Pd–Co nanoparticle size distribution (**e**) of the PdCo/MIL-53(Al)-A700 after reaction at 40 °C for 147 h on stream.

Data availability

The data used in this study are available upon request to the corresponding author.

Received: 6 August 2024; Accepted: 26 December 2024
Published online: 02 January 2025

References

1. Genest, A. et al. The origin of the particle-size-dependent selectivity in 1-butene isomerization and hydrogenation on Pd/Al_2O_3 catalysts. *Nat. Commun.* **12**, 6098–6105 (2021).
2. Alabedkhalil, A. et al. Partial hydrogenation of 1,3-butadiene over nickel with alumina and niobium supported catalysts. *Arab. J. Chem.* **17**, 105406–110430 (2024).
3. Liu, J. et al. Rational design of Pd-based alloys for 1,3-butadiene selective hydrogenation via equilibrium models of nanoparticles. *ACS Catal.* **14**, 5924–5935 (2024).
4. Yan, Z. et al. Theoretical study the influence of partial substitute noble metal Pd/Ag of PdAg-based catalyst by non-noble metal Ni/Cu for 1,3-butadiene hydrogenation. *Appl. Surf. Sci.* **588**, 152897–152903 (2022).
5. Qi, L., Dai, J., Liao, Y., Tian, J. & Sun, D. Tuning the electronic property of Pd nanoparticles by encapsulation within ZIF-67 shells towards enhanced performance in 1,3-butadiene hydrogenation. *Catal. Sci. Technol.* **12**, 2519–2530 (2022).
6. Chen, Z. et al. Carbonaceous deposits on cobalt particles reverse the catalytic patterns in butadiene hydrogenation. *Catal. Sci. Technol.* **13**, 968–974 (2023).
7. Dong, S. et al. Interstitial catbon in Ni enables high-efficiency hydrogenation of 1,3-butadiene. *Acta Phys. Chim. Sin.* **39**(11), 2301012–2301018 (2023).
8. Xu, J., Guo, X., Guan, Y. & Wu, P. Influence of Pd deposition pH value on the performance of $Pd\text{-}CuO/SiO_2$ catalyst for semi-hydrogenation of 2-methyl-3-butyn-2-ol (MBY). *Chin. Chem. Lett.* **33**, 349–353 (2022).
9. Asedegbega-Nieto, E. et al. Dynamics of Pd subsurface hydride formation and their impact on the selectivity control for selective butadiene hydrogenation reaction. *Nanomaterials* **13**, 1099–1108 (2023).
10. Yan, Y. Q. et al. H_2-free semi-hydrogenation of butadiene by the atomic sieving effect of Pd membrane with tree-like Pd dendrites array. *Angew. Chem. Int. Ed.* **135**(38), e202309013 (2023).
11. Cao, X. X. et al. Preparation and investigation of Pd doped Cu catalysts for selective hydrogenation of acetylene. *Front. Chem. Sci. Eng.* **14**, 522–533 (2019).
12. Corstius, O. E. B. et al. Mass transport effects in gas-phase selective hydrogenation of 1,3-butadiene over supported Pd. *React. Chem. Eng.* **9**, 1726–1738 (2024).
13. Wang, Y. et al. Host-induced alteration of the neighbors of single platinum atoms enables selective and stable hydrogenation of butadiene. *Nanoscale* **14**, 10506–10513 (2022).
14. Castillejos-López, E., Agostini, G., Di Michel, M., Iglesias-Juez, A. & Bachiller-Baeza, B. Synergy of contact between ZnO surface planes and PdZn nanostructures: morphology and chemical property effects in the intermetallic sites for selective 1,3-butadiene hydrogenation. *ACS Catal.* **7**, 796–811 (2017).
15. Sheng, J. et al. Porous octahedral PdCu nanocages as highly efficient electrocatalysts for the methanol oxidation reaction. *J. Mater. Chem. A* **6**, 3906–3912 (2018).
16. Gong, N. et al. Insights into the electronic modulation of bimetallic Pt-Sn cluster for the selective hydrogenation of 1,3-butadiene. *Catal. Sci. Technol.* **13**, 3313–3320 (2023).
17. Winter, L. et al. Tailoring the selectivity of 1,3-butadiene versus 1-butene adsorption on Pt(111) by ultrathin ionic liquid films. *ACS Catal.* **13**, 10866–10877 (2023).
18. Bartlewicz, O., Dąbek, I., Szymanska, A. & Maciejewski, H. Heterogeneous catalysis with the participation of ionic liquids. *Catalysts* **10**(11), 1227–1246 (2020).
19. Shophia Lawrence, A., Martin, N., Sivakumar, B., Cirujano, F. G. & Dhakshinamoorthy, A. Palladium-based metal organic frameworks as heterogeneous catalysts for C−C couplings. *ChemCatChem* **14**, e202200403 (2022).
20. Li, X. T., Chen, L., Shang, C. & Liu, Z. P. In situ surface structures of PdAg catalyst and their influence on acetylene semi-hydrogenation revealed by machine learning and experiment. *J. Am. Chem. Soc.* **143**, 6281–6292 (2021).
21. Bachiller-Baeza, B., Iglesias-Juez, A., Agostini, G. & Castillejos-López, E. Pd-Au bimetallic catalysts supported on ZnO for selective 1,3-butadiene hydrogenation. *Catal. Sci. Technol.* **10**, 2503–2512 (2020).
22. Yan, Z. et al. Theoretical study the catalytic performance and mechanism of novel designed single atom catalysts M1/2DMs for 1,3-butadiene hydrogneation. *Appl. Surf. Sci.* **617**, 156585–156596 (2023).
23. Liu, W. et al. Unveiling the Ir single atoms as selective active species for the partial hydrogenation of butadiene by operando XAS. *Nanoscale* **14**, 7641–7649 (2022).
24. Ma, H. W. et al. Understanding composition-dependent catalytic performance of PdAg for the hydrogenation of 1,3-butadiene to 1-butene. *Catal. Commun.* **149**, 106255–106260 (2021).
25. Wang, W. Y. et al. The role of adsorbed species in 1-butene isomerization: Parahydrogen-induced polarization NMR of Pd-Au catalyzed butadiene hydrogenation. *ACS Catal.* **14**(4), 2522–2531 (2024).
26. Liu, L. et al. Comparative study of Pd-Ni bimetallic catalysts supported on UiO-66 and $UiO\text{-}66\text{-}NH_2$ in selective 1,3-butadiene hydrogenation. *Nanomaterials* **12**, 1484–1498 (2022).
27. Liu, Y. et al. MOF-derived ZrO_2-supported bimetallic Pd–Ni catalyst for selective hydrogenation of 1,3-butadiene. *Molecules* **29**, 2217–2233 (2024).
28. Corstius, O. E. B. et al. Tuneable bimetallic $Pd_xCu_{100\text{-}x}$ catalysts for selective butadiene hydrogenation. *Catal. Today* **441**, 114877–114886 (2024).
29. Sun, J. D. et al. Isoprene selective hydrogenation using AgCu-promoted Pd nanoalloys. *Faraday Discuss.* **242**, 418–428 (2023).
30. Pattamakomsan, K. et al. Selective hydrogenation of 1,3-butadiene over Pd and Pd-Sn catalysts supported on different phases of alumina. *Catal. Today* **164**(1), 28–33 (2011).
31. Liu, L. et al. Bimetallic Au-Pd alloy nanoparticles supported on MIL-101(Cr) as highly efficient catalysts for selective hydrogenation of 1,3-butadiene. *RSC Adv.* **10**, 33417–33427 (2020).
32. Hossain, S. S. et al. Bimetallic Pd-Co nanoparticles supported on nitrogen-doped reduced graphene oxide as efficient electrocatalysts for formic acid electrooxidation. *Catalysts* **11**, 910–926 (2021).
33. Li, X. et al. Cellulose nanocrystal-supported Pd-Co bimetallic catalyst for selective hydrogenation of 3-nitrostyrene. *ChemNanoMat* **8**, e202200059 (2022).
34. Luo, J. et al. Pd/Co catalyst with high Pd atom utilization efficiency for nitrobenzene hydrogenation at room temperature: experimental and DFT studies. *Chem. Eur. J.* **29**, e202203142 (2023).
35. Li, H. et al. Biochar supported Ni/Fe bimetallic nanoparticles to remove 1,1,1-trichloroethane under various reaction conditions. *Chemosphere* **169**, 534–541 (2017).
36. Wang, J. et al. Halloysite-based nanomotors with embedded palladium nanoparticles for selective benzyl alcohol oxidation. *ACS Appl. Nano Mater.* **5**, 12806–12816 (2022).
37. Liu, L. et al. Heterogeneous bimetallic Cu–Ni nanoparticle-supported catalysts in the selective oxidation of benzyl alcohol to benzaldehyde. *Catalysts* **9**, 538–555 (2019).
38. Bouzayani, B. & Sanromán, M. Á. Polymer-supported heterogeneous fenton catalysts for the environmental remediation of wastewater. *Molecules* **29**, 2188–2210 (2024).
39. Talgatov, E. T. et al. Pd catalysts supported on mixed iron and titanium oxides in phenylacetylene hydrogenation: effect of TiO_2 content in magnetic support material. *Nanomaterials* **14**, 1392–1412 (2024).
40. Nakkalwar, S. L., Kaminwar, N. S., Patwari, S. B. & Kasralikar, H. M. Carbon microsphere supported copper nanoparticles (Cu-NP/C): a highly efficient and reusable catalyst for the synthesis of quinoxalines. *Indian J. Heterocycl. Chem.* **33**, 63–70 (2023).

41. Ma, M. Y. et al. Nickel nanoparticles supported on carbon cloth via pilsed laser deposition as an effective catalyst for urea electro-oxidation reaction. *J. Clust. Sci.* **35**, 79–90 (2024).
42. Galindo-Uribe, C. D., Geudtner, G., Calaminici, P. & Solorza-Feria, O. One-pot graphene supported Pt_3Cu nanoparticles—from theory towards an effective molecular oxygen reduction reaction catalyst. *Molecules* **28**, 5072–5090 (2023).
43. Liu, Z. et al. A new cobalt metal-organic framework as a substrate for Pd nanoparticles applied in high-efficiency nitro phenol degradation and cinnamaldehyde hydrogenation. *Dalton Trans.* **49**, 1191–1199 (2020).
44. Tai, X. S., Zhou, X. J. & Liu, L. L. Synthesis, crystal structure and antitumor activity of a Na(I) coordination polymer based on 2-propyl-4,5-imidazoledicarboxylic acid and 1,10-phenanthroline ligands. *Chin. J. Struct. Chem.* **38**(7), 1079–1085 (2019).
45. Zhou, X. J. et al. Two d^{10} luminescent metal–organic frameworks as dual functional luminescent sensors for (Fe^{3+}, Cu^{2+}) and 2, 4, 6-trinitrophenol (TNP) with high selectivity and sensitivity. *RSC Adv.* **10**(8), 4817–4824 (2020).
46. Tai, X. S., Yan, X. H. & Wang, L. H. Synthesis, structural characterization, hirschfeld surface analysis, density functional theory, and photocatalytic CO_2 reduction activity of a new Ca(II) complex with a bis-schiff base ligand. *Molecules* **29**(5), 1047–1056 (2024).
47. Lu, J. T., Zeng, Y., Ma, X. X., Wang, H. Q. & Meng, Q. G. Cobalt nanoparticles embedded into N-doped carbon from metal organic frameworks as highly active electrocatalyst for oxygen evolution reaction. *Polymers* **11**(5), 828–836 (2019).
48. Xin, C. L. et al. Enhancement of hydrothermal stability and CO_2 adsorption of Mg-MOF-74/MCF composites. *ACS Omega* **6**(11), 7739–7745 (2021).
49. Neon, L. B., Drobek, M., Bechelany, M., Rebiere, B. & Julbe, A. Microwaves induced epitaxial growth of urchin like MIL-53(Al) crystals on ceramic supports. *Sci. Rep.* **14**, 20067–20074 (2024).
50. Metawea, R., Farag, H. A., El-Ashtoukhy, E. S., El-latif, M. M. & El-Sayed, E. M. Ultrasounds assisted one-pot oxidative desulfurization of model fuel using green synthesized aluminum terephthalate [MIL-53(Al)]. *Sci. Rep.* **13**, 13728–13737 (2023).
51. Wang, S. et al. Construction of a highly active and water-resistant Ni-based catalyst for the HDO reaction of phenol. *Sustain. Energy Fuels* **6**, 4183–4196 (2022).
52. Li, Q. et al. Efficient infrared-light-driven photothermal CO_2 reduction over MOF-derived defective Ni/TiO_2. *Appl. Catal. B Environ.* **303**, 120905–120915 (2022).
53. Jia, H., Xie, R., Lu, G., Jiang, H. & Zhang, M. Direct construction of julolidines via reductive annulation of quinolines and conjugated enones by a MOF-derived hierarchically porous iridium catalyst. *ACS Catal.* **12**, 10294–10303 (2022).
54. Mei, J. et al. Surfactant-assisted synthesis of MOF-derived CeO_2 for low-temperature catalytic o-xylene combustion. *J. Environ. Chem. Eng.* **10**, 108743–108751 (2022).
55. Liu, L., Tai, X., Zhang, N., Meng, Q. & Xin, C. Supported Au/MIL-53(Al): a reusable green solid catalyst for the three-component coupling reaction of aldehyde, alkyne, and amine. *Reac. Kinet. Mech. Cat.* **119**, 335–348 (2016).
56. Liu, L. L. et al. Au–Pt bimetallic nanoparticle catalysts supported on UiO-67 for selective 1, 3-butadiene hydrogenation. *J. Taiwan Inst. Chem. E* **114**, 220–227 (2020).
57. Wang, W. et al. MIL-53(Al) derived single-atom Rh catalyst for the selective hydrogneation of *m*-chloronitrobenzene into *m*-chloroaniline. *Chin. J. Catal.* **42**, 824–834 (2021).
58. Su, J., Jia, Y., Shi, M., Shen, K. & Zhang, J. Highly efficient unsymmetrical dimethylhydrazine removal from wastewater using MIL-53(Al)-derived carbons: adsorption performance and mechanisms exploration. *J. Environ. Chem. Eng.* **10**, 108975–108987 (2022).
59. Sridevi, A., Krishnamohan, S., Thairiyaraja, M., Prakash, B. & Yokeshwaran, R. Visible-light driven γ-Al_2O_3, CuO, and γ-Al_2O_3/CuO nanocatalysts: synthesis and enhanced photocatalytic activity. *Inorg. Chem. Commun.* **138**, 109311–109323 (2022).
60. Lv, J., Chen, C., Guo, X., Ding, W. & Yang, W. Crystal facet effect of γ-Al_2O_3 on catalytic property of CuO/γ-Al_2O_3 for CO oxidation. *Mol. Catal.* **547**, 113405–113410 (2023).
61. Du, C. B., Tu, J. Y., Law, Z. X. & Tsai, D. H. Aerosol metal-organic framework-derived Ni-Zn-Al hybrid catalyst for efficient methane bi-reforming. *Int. J. Hydrogen Energy* **57**, 1152–1163 (2024).
62. Tang, C., Feng, Z. & Bai, X. Magnetic N-doped partially graphitized carbon-loaded Pd-Co alloy nanoparticles for efficient hydrogen production. *Colloid Surface A* **648**, 129348–129358 (2022).
63. Yang, J., Wang, W. D. & Dong, Z. PdCo nanoparticles supported on carbon fibers derived from cotton: maximum utilization of Pd atoms for efficient reduction of nitroarenes. *J. Colloid Interf. Sci.* **524**, 84–92 (2018).
64. Thirugalathi Anbalagan, R. et al. Carbonaceous nanocomposites decorated with Pd-Co alloy as catalyst for hydrogen evolution reaction. *Ionics* **30**(1), 445–455 (2024).
65. Kottayintavida, R., Ganguly, D. & Gopalan, N. K. Bimetallic $NiWO_4$ as an efficient interface modulator for Pd towards enhanced alcohol electro-oxidation. *Electrocatalysis* **15**, 191–203 (2024).
66. Wu, M. et al. Elucidation of the active phase in Pd-based catalysts supporting on octahedral CeO_2 for low-temperature methane oxidation. *ChemistrySelect* **6**, 4149–4159 (2021).
67. Huang, Z. et al. Enhancing CH_4/N_2 separation performance within aluminum-based metal-organic frameworks: influence of the pore structure and linker polarity. *Sep. Purif. Technol.* **286**, 120446–120454 (2021).
68. Pitayachinchot, H., Reubroycharoen, P., Prasassarakich, P. & Ngamcharussrivichai, C. Highly selective iron-based catalysts derived from Al-containing MIL-53 for CO_2 hydrogenation to light olefins. *J. Environ. Chem. Eng.* **12**, 112061–112070 (2024).
69. Liu, L. et al. MIL-100(Fe) supported PtCo nanoparticles as active and selective heterogeneous catalysts for hydrogenation of 1,3-butadiene. *ChemistryOpen* **11**, e202100288 (2022).
70. Liu, L. et al. Bimetallic Au-Ni alloy nanoparticles in a metaleorganic framework (MIL-101) as efficient heterogeneous catalysts for selective oxidation of benzyl alcohol into benzaldehyde. *J. Alloy. Compd.* **780**, 326–336 (2019).
71. Gao, S. T., Liu, W., Feng, C., Shang, N. Z. & Wang, C. A Ag-Pd alloy supported on an amine-functionalized UiO-66 as an efficient synergetic catalyst for the dehydrogenation of formic acid at room temperature. *Catal. Sci. Technol.* **6**, 869–874 (2016).
72. Liu, L. et al. ZIF-67 supported Pd nanoparticles and Pd-Cu nanoparticles for selective hydrogenation of 1,3-butadiene. *Acta Mater. Compos. Sin.* **39**(7), 3376–3387 (2022).
73. Wu, J., Zuo, J., Liu, K., Lin, J. & Liu, Z. Highly active/selective synergistic catalysis of bimetallic Pd/Co catalyst anchored on air-mediated nanocarbons for H_2 production by formic acid dehydrogenation. *Catal. Lett.* **153**, 2517–2526 (2023).
74. Wu, S. et al. Quantifying the photocatalytic role and activity at the edge and surface of Pd co-catalysts using N_2 fixation as a case. *J. Mater. Chem. A* **9**, 26036–26044 (2021).
75. Lin, J., Chen, J. & Su, W. Rhodium-cobalt bimetallic nanoparticles: A catalyst for selective hydrogenation of unsaturated carbon-carbon bonds with hydrous hydrazine. *Adv. Synth. Catal.* **355**, 41–46 (2013).
76. An, Q. et al. Sandwich structured aryl-diimine Pd(II)/Co(II) monolayer-fabrication, catalytic performance, synergistic effect and mechanism investigation. *Mol. Catal.* **501**, 111359–111348 (2021).
77. Yuan, E. et al. Constructing a Pd–Co interface to tailor a d-band center for highly efficient hydroconversion of furfural over cobalt oxide-supported Pd catalysts. *ACS Appl. Mater. Inter.* **15**, 43845–43858 (2023).
78. Miao, Y. et al. Single-atomic-Co cocatalyst on (040) facet of $BiVO_4$ toward efficient photoelectrochemical water splitting. *Chem. Eng. J.* **427**, 131011–131019 (2022).
79. Xu, Y. et al. Plant-mediated synthesis of Pd catalysts toward selective hydrogenation of 1,3-butadiene: The effect of halide ions. *Ind. Eng. Chem. Res.* **56**, 10623–10630 (2017).
80. Hou, R., Porosoff, M. D., Chen, J. G. & Wang, T. Effect of oxide supports on Pd–Ni bimetallic catalysts for 1,3-butadiene hydrogenation. *Appl. Catal. A Gen.* **490**, 17–23 (2015).
81. Xia, C. et al. General synthesis of single-atom catalysts with high metal loading using graphene quantum dots. *Nat. Chem.* **13**, 887–894 (2021).

82. Decarolis, D., Lezcano-Gonzalez, I., Gianolio, D. & Beale, A. M. Effect of particle size and support type on Pd catalysts for 1, 3-butadiene hydrogenation. *Top. Catal.* **61**, 162–174 (2018).
83. Lin, H. et al. Bimetallic nanoparticles: advances in fundamental investigations and catalytic applications. *Environ. Sci. Adv.* https://doi.org/10.1039/d4va00241e (2024).
84. Ji, L. et al. Synergistic effect and role of light for efficient photothermocatalytic CO_2 reduction by CH_4 on Pd/Co-$Al_1Mg_3O_x$. *Appl. Catal. B Environ. Energy* **361**, 124689–124700 (2025).
85. Rai, R. K., Tyagi, D., Gupta, K. & Singh, S. K. Activated nanostructured bimetallic catalysts for C-C coupling reactions: recent progress. *Catal. Sci. Technol.* **6**, 3341–3361 (2016).
86. Yu, L. et al. Synthesis of PtCuFe alloy nanoframes with high-index facets and enhanced electrocatalytic properties. *Fuel* **315**, 123280–123291 (2022).
87. Liu, L. L. et al. Efficient oxidation of benzyl alcohol into benzaldehyde catalyzed by graphene oxide and reduced graphene oxide supported bimetallic Au–Sn catalysts. *RSC Adv.* **13**(34), 23648–23658 (2023).
88. Sobhani, S., Zarei, H. & Sansano, J. M. A new nanomagnetic Pd-Co bimetallic alloy as catalyst in the Mizoroki-Heck and Buchwald-Hartwig amination reactions in aqueous media. *Sci. Rep.* **11**, 17025–17045 (2021).
89. Wu, W. H. et al. Alloying effect enhanced bimetallic Ni-Fe/TiO_2 catalysts for selective hydrogenation of 1,3-butadiene in the presence of an excess of propylene. *Mol. Catal.* **550**, 113602–113612 (2023).
90. Yu, W., Yan, J., Cui, Z. & Yang, N. Preparation of mesoporous Cu/Zn/Ce/Zr/Al catalysts and activity in steam reforming of methanol. *AIP Adv.* **11**, 125230–125240 (2021).
91. Kumar, A., Vikrant, K., Younis, S. A. & Kim, K. H. Tuning of active nickel species in MOF-derived nickel catalysts for the control on acetic acid steam reforming and hydrogen production. *Int. J. Hydrogen Energy* **48**, 14964–14977 (2023).

Acknowledgements

This research was funded by National Natural Science Foundation of China (grant number 21802104) and the Natural Science Foundation of Shandong Province (grant number ZR2017MB056).

Author contributions

L.L. (Lili Liu) wrote the main manuscript text and carried out editing. M.Z., L.L. (Lei Li), Y.Z. and L.W. were carried out experiments and characterization of the samples. X.Z., C.X., and X.T. conceived the scientific idea and carried out supervision activity. All authors reviewed the manuscript and participated in the formal analysis of data.

Declarations

Competing interests

The authors declare no competing interests.

Additional information

Supplementary Information The online version contains supplementary material available at https://doi.org/10.1038/s41598-024-84707-3.

Correspondence and requests for materials should be addressed to L.L., C.X. or X.T.